RSC Advances

PAPER

View Article Online
View Journal | View Issue

Cite this: *RSC Adv.*, 2021, **11**, 30623

Biocidal activity of Ba^{2+}-doped CeO_2 NPs against *Streptococcus mutans* and *Staphylococcus aureus* bacterial strains†

Natarajan Sisubalan,[a] Chandrasekaran Karthikeyan,*[bc] Venugopal Senthil Kumar,[c] Kokkarachedu Varaprasad,*[b] Abdulrahman Syed ahamed Haja Hameed,[d] Ramar Vanajothi[e] and Rotimi Sadiku[f]

Mishandling of antibiotics often leads to the development of multiple drug resistance (MDR) among microbes, resulting in the failure of infection treatments and putting human health at great risk. As a response, unique nanomaterials with superior bioactivity must be developed to combat bacterial infections. Herein, CeO_2-based nanomaterials (NMs) were synthesized by employing cerium(III) nitrate and selective alkaline ions. Moreover, the influence of alkaline ions on CeO_2 was investigated, and their characteristics, *viz.*: biochemical, structural, and optical properties, were altered. The size of nano Ba-doped CeO_2 (BCO) was ~2.3 nm, relatively smaller than other NMs and the antibacterial potential of CeO_2, Mg-doped CeO_2 (MCO), Ca-doped CeO_2 (CCO), Sr-doped CeO_2 (SCO), and Ba-doped CeO_2 (BCO) NMs against *Streptococcus mutans* (*S. mutans*) and *Staphylococcus aureus* (*S. aureus*) strains was assessed. BCO outperformed all NMs in terms of antibacterial efficacy. In addition, achieving the enhanced bioactivity of BCO due to reduced particle size facilitated the easy penetration into the bacterial membrane and the presence of a sizeable interfacial surface. In this study, the minimum quantity of BCO required to achieve the complete inhibition of bacteria was determined to be 1000 μg mL^{-1} and 1500 μg mL^{-1} for *S. mutans* and *S. aureus*, respectively. The cytotoxicity test with L929 fibroblast cells demonstrated that BCO was less toxic to healthy cells. Furthermore, BCO did not show any toxicity and cell morphological changes in the L929 fibroblast cells, which is similar to the control cell morphology. Overall, the results suggest that nano BCO can be used in biomedical applications, which can potentially help improve human health conditions.

Received 5th August 2021
Accepted 27th August 2021

DOI: 10.1039/d1ra05948c

rsc.li/rsc-advances

Introduction

In recent years, multidrug resistance (MDR) in pathogenic bacteria has been a severe health concern to humanity.[1,2] The humanoid community has remained unaware or failed to understand the undeniable truth that drug misuse, underuse, or overuse (abuse) of antibiotics might increase microbial resistance, which often negatively impact their efficacy.[3,4] The tendency of bacteria to develop resistance against allopathic antibiotics customarily makes these drugs lose their efficiency over time, thereby putting millions of lives in jeopardy.[5] Even though techno-universe pharmaceutical (biomedical) innovations have continuously and relentlessly been developed, it is undeniably concerning that healthcare-related infections are one of the central origins of disease in the United States of America and other countries. *Candida albicans* (*C. albicans*) and *Staphylococcus aureus* (*S. aureus*) are among the most general microbes linked to healthcare-related infections.[6] Accordingly, it is urgent to design novel drugs against rapidly growing MDR bacterial infections. CeO_2 NPs have recently attracted the attention of researchers because of their promising usage in biomedical applications, such as radiation therapy, chemotherapy, treating neurodegenerative disorders, cardiovascular diseases, Alzheimer's disease, sepsis therapies, and antibacterial infections, due to their antioxidant properties toward reactive oxygen species (ROS).[7] CeO_2 NPs can be produced using various chemical methods, including chemical precipitation, precipitation, microwave hydrothermal,

[a]*Department of Botany, Bishop Heber College, Affiliated to Bharathidasan University, Trichy 620017, Tamil Nadu, India*

[b]*Centro de Investigaciòn de Polimeros Avanzados (CIPA), Avendia Collao 1202, Edificio de Laboratorios de CIPA, Concepciòn, Chile. E-mail: prasad@cipachile.cl; karthiisro@gmail.com*

[c]*KIRND Institute of Research and Development PVT LTD, Tiruchirappalli 620020, Tamil Nadu, India. E-mail: varmaindian@gmail.com*

[d]*PG and Research Department of Physics, Jamal Mohamed College (Affiliated to Bharathidasan University), Tiruchirappalli, Tamil Nadu, 620 020, India*

[e]*Department of Zoology, Fatima College, Madurai 625001, Tamil Nadu, India*

[f]*Institute of NanoEngineering Research (INER), Department of Chemical, Metallurgical & Materials Engineering (Polymer Division), Tshwane University of Technology, Pretoria West Campus, Staatsarillerie Rd, Pretoria, 1083, South Africa*

† Electronic supplementary information (ESI) available. See DOI: 10.1039/d1ra05948c

reverse-co-precipitation, and sonochemical methods. The reported properties of the NPs synthesized using these methods, however, are inconsistent. Since the size and composition of synthesized CeO_2 NPs are critical to their success, it is essential to use processes that constantly generate materials with advanced properties. Multiple techniques, including a precipitation process and a microwave hydrothermal technique, have outperformed others due to their advanced multifunctional properties.[7]

The usage of CeO_2 NPs in pharmaceutical applications has recently gained attention because they resist cell damage caused by toxicants, radiation and microbial communities, neurological disorders, brain/heart ischemia, and retinal neurodegeneration. Cerium has a fluorite structure in its oxide form. The CeO_2 NPs, with their nanoscale shape, maintain the fluorite structure despite oxygen deficiency. That is, CeO_2 NPs with (CeO_{2-x}) vacancies are formed, thereby providing sites for reduction–oxidation reactions. The catalytic efficiency of the NPs is determined by the arrangement of the surfaces of the fluorite structure. CeO_2 NPs are inexpensive and retain their catalytic properties even when exposed to extreme temperatures. They have strong SOD-like behaviour even though they are not naturally occurring enzymes. Therefore, they act as a biocompatible alternative to natural bio-scavengers, like superoxide dismutase, because of their ability to scavenge reactive oxygen species in an enzyme-like manner. The non-stoichiometric oxygen ratio of Ce^{3+}/Ce^{4+} on the surface of the nanostructures changes, when CeO_2 nanostructures are formed.[8] This unique characteristic confers the radical scavenging assets on CeO_2 NMs, making them an attractive choice for biomedical applications in advanced healthcare. CeO_2 NMs invade bacterial cell membranes and bind them to the mesosomes, thus disrupting the mesosomal functions, including respiration of cell, replication of deoxyribonucleic acid (DNA) and cell division; therefore, the bacterial cell membrane surface area is increased. The ROS cause more oxidative stress to the bacterial cellular components due to cell expiration established by this intracellular functional change.[9] Moreover, CeO_2 NPs display a crucial antimicrobial action since they act as scavengers of radicals and block ROS generation, which may conjointly eradicate the microorganisms.[10] In addition, CeO_2 NMs enhance the effectiveness of medicines towards the microbial cell membrane changes because the ions in the Ce^{4+} oxidative state close to the membrane surface reduce to the Ce^{3+} oxidative state.[11] However, the antibacterial and antioxidant nature and toxicity of MCO, CCO, SCO, and BCO NMs have not been reported earlier.

With the addition of alkaline metals onto the surfaces of CeO_2 matrices, which can change the optical and biocidal properties of nanomaterials, due to bandgap illumination, the electrons (e^-) of NMs are excited *via* the bandgap to the conduction band, producing holes (h^+) in the valence band.[12] As a result, the conduction band electrons and the valence band holes produce highly active reducing and oxidizing agents. These oxidizing agents ($^{\bullet}OH$ and $^{\bullet}O_2^-$) are responsible for the antibacterial activity of CeO_2 NPs, which could be altered by doping the CeO_2 NPs with alkali metal ions (AMIs) because they (Ba ions) act as electron traps that can inhibit the rate of e^-/h^+ pair recombination by augmenting the bandgap energy. This stimulates the formation of ROS and increases the antibacterial efficacy.[13] In this study, the antibacterial properties of CeO_2, MCO, CCO, SCO, and BCO NMs against *S. mutans* and *S. aureus* strains were studied *via* optical and structural characterization to explore their potential as futuristic medicines/antibiotic agents that can overcome antimicrobial-resistant infections. Mainly, barium atoms enhanced the antibacterial activity, toxicity, and antioxidant and biocidal properties of CeO_2.

Experimental methods

Synthesis of nanomaterials

The following high-purity chemicals were used as source materials: $Ce(NO_3)_3\cdot 6H_2O$, $Mg(NO_3)_2\cdot 6H_2O$, $Ca(NO_3)_2\cdot 4H_2O$, $Ba(NO_3)_2$, $Sr(NO_3)_2$, monoethanolamine and NaOH.

The method of synthesis of CeO_2, MCO, CCO, SCO, and BCO NMs was as follows: 0.1 M of $Ce(NO_3)_3\cdot 6H_2O$, 0.8 M of NaOH and 3.008 mL of monoethanolamine were dissolved one by one in 100 mL of deionized water in three 200 mL beakers for the synthesis of CeO_2 NPs. First, a violet precipitate was obtained with the dropwise addition of a NaOH solution into the homogenous cerium nitrate and monoethanolamine solution. Then, the violet precipitate solution was stirred for 24 h at 25 ± 2 °C, and the colour of the solution changed from a violet precipitate to a yellow residue after 6 h. After that, a stable, transparent solution was obtained, and the precipitate solution was washed repeatedly with deionized water and ethanol. Finally, at 120 °C, the precipitate was dried completely to obtain CeO_2 NPs.

Likewise, a 0.005 M aqueous solution of magnesium nitrate hexahydrate was mixed with a 0.095 M aqueous cerium nitrate solution to synthesize MCO. In 100 mL of a metal solution containing 3.008 mL of monoethanolamine, this solution was mixed. To this homogenous mixture, 0.8 M of aqueous NaOH solution was mixed dropwise, forming a violet precipitate. The solution was modified to a yellow residue, which was treated as mentioned above to obtain MCO NMs. Similar steps were repeated to prepare the CeO_2 NPs amalgamated with Sr, Ca, and Ba for which strontium nitrate, calcium nitrate tetrahydrate, and barium nitrate were used, respectively. The pure and AMIs-amalgamated CeO_2 NPs (AMI) were obtained. These NMs were calcinated for 5 h at 700 °C and then used for further tests.

Characterization (ESI†). The details on the characterization, antibacterial activity assay, and MIC and MBC measurements of the NMs are provided in ESI.†

Results and discussion

The non-toxic CeO_2-based NMs with biocidal activities were developed *via* a precipitation method. This method enhanced the biocidal properties *via* modifications of the CeO_2 NMs using AMIs. The XRD patterns of the CeO_2 (pure), MCO, CCO, SCO, and BCO NMs are shown in Fig. 1a. Eight identical O_2^- ions surrounded the fluorite crystal structure of the CeO_2 NPs; each O_2^- coordinated with four Ce^{4+} ions, materializing the edge of a square.[14,15] The (111), (200) and (220) crystal planes of CeO_2 NPs were located at the diffraction Bragg's angles (2θ) of 28.60,

33.11 and 47.58°, respectively. Similarly, at the 2θ angles of 56.34 and 76.6°, peaks corresponding to the (311) and (331) planes of CeO_2 NPs, other peaks were located. The CeO_2 peaks corresponded with the CeO_2 cubic fluorite crystal structure (JCPDS-340394).[14,15]

MCO, CCO, SCO, and BCO showed increased crystalline nature compared with pure CeO_2 NPs. The diffraction angles (2θ) were found to be (28.66, 33.16, 47.60, 56.40 & 76.93°), (28.62, 33.0, 47.52, 56.37& 76.9°), (28.5, 33.04, 47.46, 56.29, 69.3, 76.93 & 78.91°) and (28.53, 33.09, 47.50, 56.32, 69.04 & 76.9°) for MCO, CCO, SCO, and BCO, respectively. Due to the small ionic radii of the Mg^{2+} (0.66 Å), Ca^{2+} (0.99 Å), Sr^{2+} (1.13 Å) and Ba^{2+} (1.35 Å) ions when amalgamated with CeO_2 NMs, it was found that the ionic radius of pure Ce^{3+} was 1.14 Å, without any impurity phase in MCO, CCO, SCO, and BCO. In the literature, Lee *et al.* have reported that the formation of La-doped CeO_2 NPs in the trivalent state was due to the presence of the Ce L-edge, signifying that the valence state of Ce varied between 4+ and 3+ mainly depending on the degree of oxygen deficiency.[16] Thus, the change in the valence of Ce can be identified by the Ce^{3+} state. In this work, the alkaline metal ion-doped CeO_2 NPs also displayed the Ce^{3+} state.

The lattice parameters of each NM were calculated according to the formula:

$$\frac{1}{d^2} = \left(\frac{h^2 + k^2 + l^2}{a^2}\right)$$

By re-writing the equation as $a = \sqrt{d^2(h^2 + k^2 + l^2)}$, the lattice constant '$a$' was evaluated. The obtained 'a' values were 5.4014 Å, 5.3896 Å, 5.3986 Å, 5.4140 Å and 5.5644 Å for CeO_2, MCO, CCO, SCO, and BCO, respectively. The diffraction peaks of MCO, CCO, SCO, and BCO NMs showed marginal shifts in their diffraction angles, diverging from those of the CeO_2 NPs, which resulted in variations in the lattice constants of the metal ion-doped CeO_2 NPs. These variations were attributed to the substitution of Ce (ionic radius 1.14 Å) with metals of smaller ionic radii, *viz.* Mg (0.66 Å), Ca (0.99 Å), Sr (1.13 Å) and Ba (1.35 Å). This suggested that the Mg, Ca, Sr and Ba ions were amalgamated into the CeO_2 matrix. The average crystallite size of the various NMs was measured using Debye–Scherrer's equation.

$$\text{Average crystallite size } D = \frac{k\lambda}{\beta_{D\cos\theta}}$$

The average particle sizes of the CeO_2, MCO, CCO, SCO, and BCO NMs were 5.2, 3.4, 3.0, 3.7 and 2.3 nm, respectively. The average crystal sizes of the amalgamated CeO_2 NPs had decreased compared with that of pure CeO_2 due to the bias in the main CeO_2 lattice caused by the extraneous impurities, *i.e.*, Mg^{2+}, Ca^{2+}, Sr^{2+} and Ba^{2+}, which hindered the nucleation and further growth of the CeO_2 NPs.

In Fig. 1b, the UV-vis optical reflection spectra of the CeO_2, MCO, CCO, SCO, and BCO NMs are shown. The absorption edges of the UV spectral peaks were found at ~435, ~427, ~420, ~413 and ~399 nm for the CeO_2, MCO, CCO, SCO, and BCO NMs, respectively, which endorsed the photoexcitation of electrons to the conduction band from the valence band. The peak positions in the reflection spectra of the alkaline metal ion-amalgamated CeO_2 NPs were blue-shifted towards the lower wavelength. This showed that doping with the Mg, Ca, Sr, and Ba atoms caused the bandgap of CeO_2 NPs to increase. The relationship between the coefficient of absorption (α) and the incident photon energy ($h\nu$) is expressed by the following equation:

$$\alpha h\nu = A(h\nu - E_g)^n$$

Because of the direct band transition in CeO_2 NPs and those amalgamated with metal (alkaline) ions, *i.e.*, Mg, Ca, Sr and Ba, a plot of $(\alpha h\nu)2$ *vs.* photon energy $h\nu$ was drawn, and the extrapolation of the linear portion of the absorption edge to obtain the energy-axis intercept is shown in Fig. 2(a–e). The bandgap values of 2.85, 2.9, 2.95, 3.0 and 3.1 eV were observed

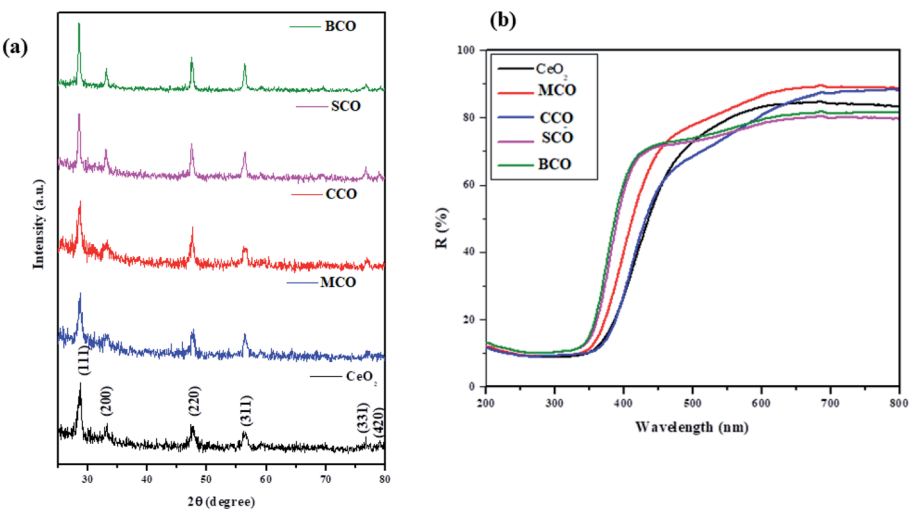

Fig. 1 (a): XRD patterns of the NMs, and (b) UV-vis reflection spectra of the CeO_2, MCO, CCO, SCO, and BCO NMs.

for pure CeO_2 NPs and the metal (alkaline) ion-doped NPs, *viz.*: MCO, CCO, SCO, and BCO NMs, respectively. The bandgap of BCO NPs was more significant than those of the pure and the other alkaline metal ion-doped CeO_2 NPs, *viz.* MCO, CCO, and SCO NMs. The valence structure and form of the conduction bands determine the optical properties of semiconductor NPs. Besides this, doping also plays a role through the Burstein–Moss (BM) effect.[17] From the XRD result, it was found that the size of the BCO (2.3 nm) NMs was smaller than those of the CeO_2 (5.2 nm), MCO (3.4 nm), CCO (3.0 nm) and SCO (3.7 nm) NMs. In small particles, the carriers are more confined, thus increasing the energy gap of the NPs. Consequently, the increase in the bandgap of the BCO NMs was due to both small particle size and the BM effect.

Photoluminescence (PL) spectroscopy

In contrast to CeO_2, the MCO, CCO, SCO and BCO NMs were anticipated to have diverse optical properties. At the exciting wavelength of 290 nm, the PL spectra of the as-synthesized CeO_2, MCO, CCO, SCO and BCO NMs were obtained. For the CeO_2, MCO, CCO, SCO and BCO NMs, the PL emission peaks were observed from 350 nm to 550 nm. For all the PL spectra, satisfactory fits with nine peaks were obtained by using the Gaussian function and labeled as: V1, V2, V3, V4, V5, V6, V7, V8 and V9, as shown in Fig. 3(a–e). The oxygen ions in the CeO_2 cubic fluorite structure were not tightly packed, resulting in many oxygen vacancies while maintaining the basic fluorite structure.[18,19] The photo-excitation mechanism in Ceria can be defined by the Kroger–Vink notation[20] as $4Ce_{Ce} + O_o 2Ce_{Ce} + 2Ce'_{Ce} + V_o + (1/2)$ of O_2 (g). The symbols in this equation have the following meanings: Ce_{ce} is a Ce^{4+} ion on a Ce lattice site, O_o is an O_2^- ion on an O lattice site, $2Ce'_{Ce}$ is a Ce^{3+} ion on a Ce lattice site and V_o is the neutral vacancy of oxygen trapped in the V_o cavity that provides the F centers. It is called the F^+ center when a single electron is trapped and denoted as the F^{++} center[21,22] when the vacancy is deficient of the electron pair. In Ceria (CeO_2), the energy levels of Ce 4f are localized at the prohibited band and remain at around 3 eV above the width of the valence band (O 2p) at 1.2 eV.[23,24] With the defect levels located on the Ce 4f band and O 2p band, they should produce broader emission bands. Fig. 2F shows a schematic depicting the UV and visible emission peaks of CeO_2.

Fig. 3a shows the PL emission spectrum of pure CeO_2 NMs, which has nine emission bands at ~399, ~420, ~441, ~451, ~468, ~482, ~492, ~509 and ~539 nm. The near-band edge emission was seen at ~399 nm, with the violet emission at ~420 nm, four blue emissions at ~441 nm, ~451 nm, ~468 nm and ~482 nm, blue-green emission at ~492 nm and two green emissions at ~509 and ~539 nm. A broad band was observed for the emission peaks between ~400 and ~550 nm. The broad near band edge emission based at 399 nm corresponded to a band-to-band recombination phase, which is likely to involve localized or free excitons.[25] The violet-blue emission bands were from the surface defect between the bands Ce 4f and O 2p.[26] The excitonic recombination of CeO_2 NMs was reflected by the blue emission band (~441 nm).[27,28] This was attributed to Ce^{3+}, 5d–4f +'s shifts between the ground states ^2D ($5d^1$) and $^2F_{5/2}$ ($4f^1$). The blue and blue-green emission bands at ~451 nm, ~469 nm, ~482 nm and ~492 nm were due to the transitions from various defect levels to the O 2p band. The green emission bands observed at 509 nm and 539 nm were due to the low density of oxygen vacancies. The positions of the V1, V2, V3, V4, V5, V6, V7, V8 and V9 emission bands of MCO, CCO, SCO and BCO NMs are

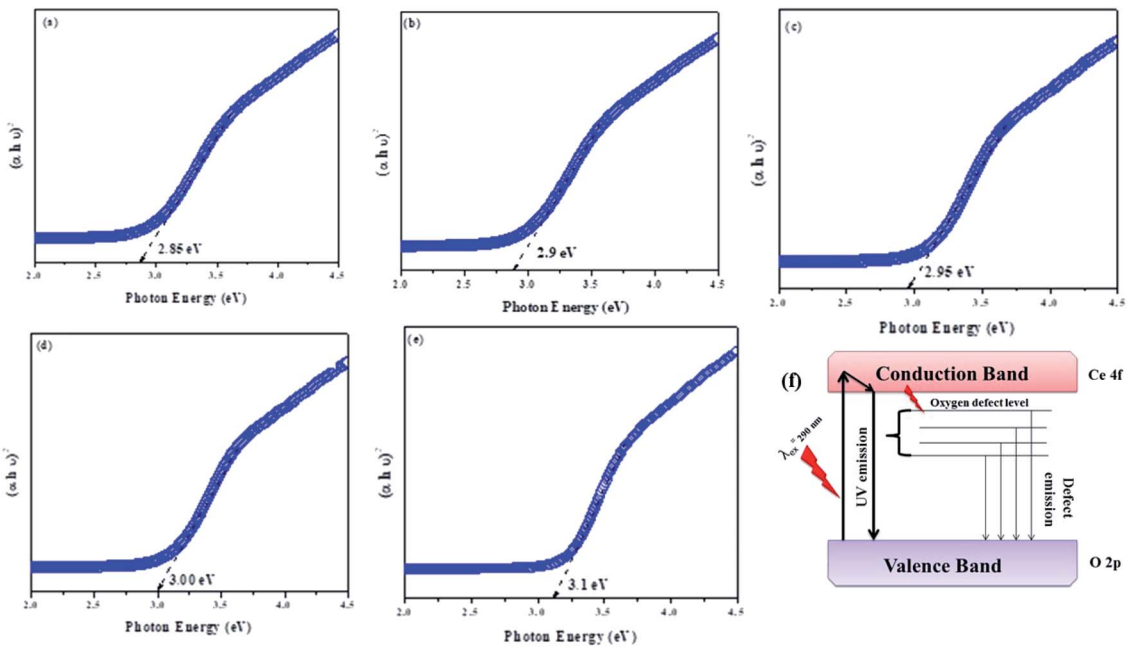

Fig. 2 (a–e) The optical bandgap energy of CeO_2, MCO, CCO, SCO and BCO NMs, and (f) the schematic of the various forms of CeO_2 NPs, showing the UV and visible emission peaks.

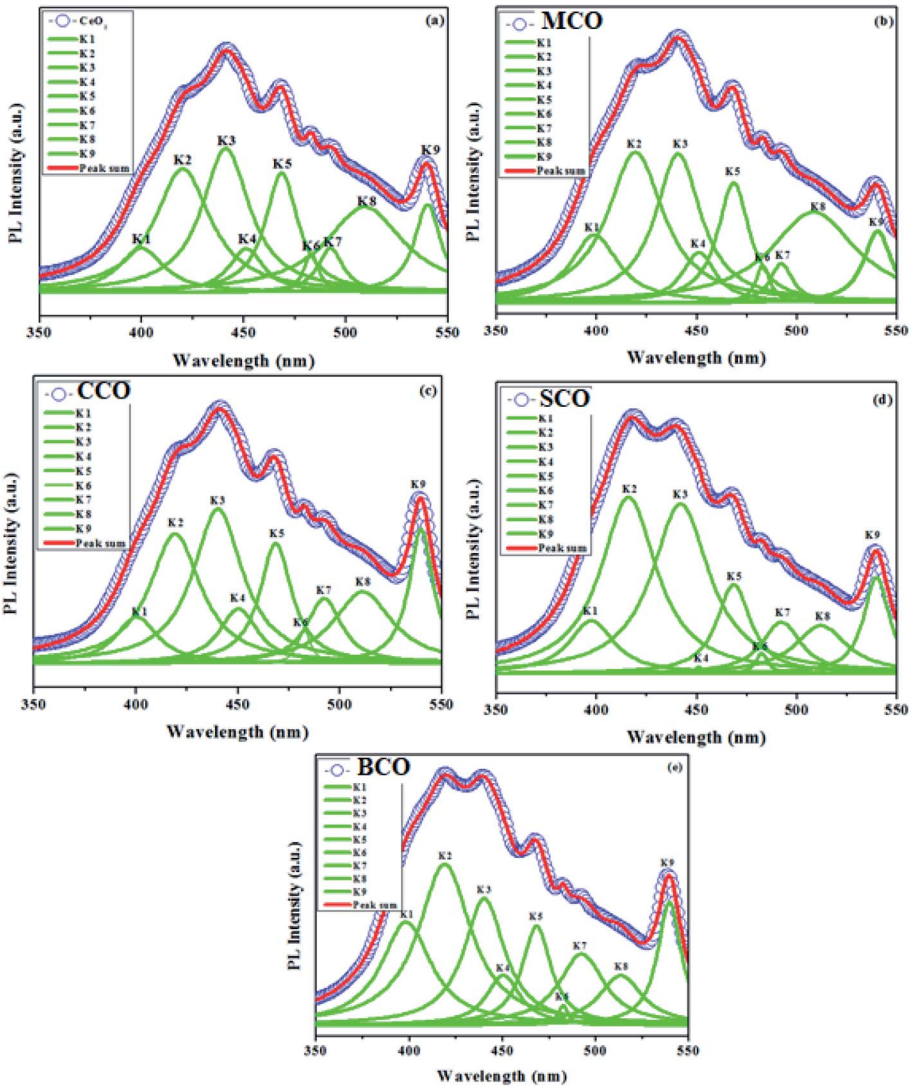

Fig. 3 PL emission spectra of the (a) CeO_2, (b) MCO, (c) CCO, (d) SCO and (e) BCO NMs.

given in Table 1. Owing to the falsification in the host CeO_2 lattice using AMIs as impurities, the violet emission wavelength of CeO_2 NMs was reduced compared with MCO, CCO, SCO and BCO NMs. The emission values of the green bands (V8 and V9) of the BCO NPs were increased compared to CeO_2, MCO, CCO, and SCO NMs. The increasing green emission yielded more oxygen vacancies, *i.e.*, a larger number of ROS, which played a vital role in the antibacterial efficiency of BCO NMs. The AMI, namely Mg^{2+}, Ca^{2+}, Sr^{2+}, and Ba^{2+}, were substituted into the CeO_2 lattice, confirming the changes in emissions.

FESEM was carried out for the morphological analysis of the CeO_2, MCO, CCO, SCO and BCO NMs, and the images are shown in Fig. 4(a–e). The synthesized CeO_2 NPs exhibited a spherical structure, and the MCO, CCO, SCO and BCO NMs formed needle-like structures with a uniform grain boundary. The average particle sizes were observed as 23, 19, 15, 13 and 10 nm for the CeO_2, MCO, CCO, SCO and BCO NMs, respectively.

The chemical composition of the CeO_2, MCO, CCO, SCO and BCO NMs was investigated by energy-dispersive X-ray analysis, as shown in Fig. 4(a1–e1). Based on the EDAX analysis, the amounts of AMIs present in the doped CeO_2 NMs are given in Table 2. In the MCO, CCO, SCO and BCO NMs, the metal concentrations were observed at 1.56% Mg, 2.64% Ca, 1.06% Sr and 1.84% Ba, respectively. In CeO_2 NPs, the atomic percentages of Ce and O were observed at 36.80% and 63.20%, respectively.

In the MCO and CCO NMs, the cerium content increased, whereas the oxygen content reduced. In the CeO_2 NMs doped with calcium, the levels of Ce and O were calculated to be 49.30% and 48.05%, respectively. A similar trend to the CeO_2 NPs was observed in the chemical composition of the CCO NMs. However, the cerium percentage decreased for the SCO and BCO NMs, and the oxygen percentage increased. In the CeO_2 NPs doped with Ba, the proportions of Ce and O were observed to be 24.59% and 73.57%, respectively. The atomic percentages of Ce and O were found to increase than the CeO_2 NMs due to

Table 1 The PL emission values of the CeO_2, MCO, CCO, SCO and BCO NMs

Peak position	CeO_2 (nm)	MCO (nm)	CCO (nm)	SCO (nm)	BCO (nm)
V1	399	398	400	397	398
V2	420	419	419	415	418
V3	441	440	440	441	440
V4	451	451	450	450	450
V5	468	468	468	468	468
V6	482	482	482	482	482
V7	492	492	492	492	492
V8	509	508	511	512	513
V9	539	538	539	539	542

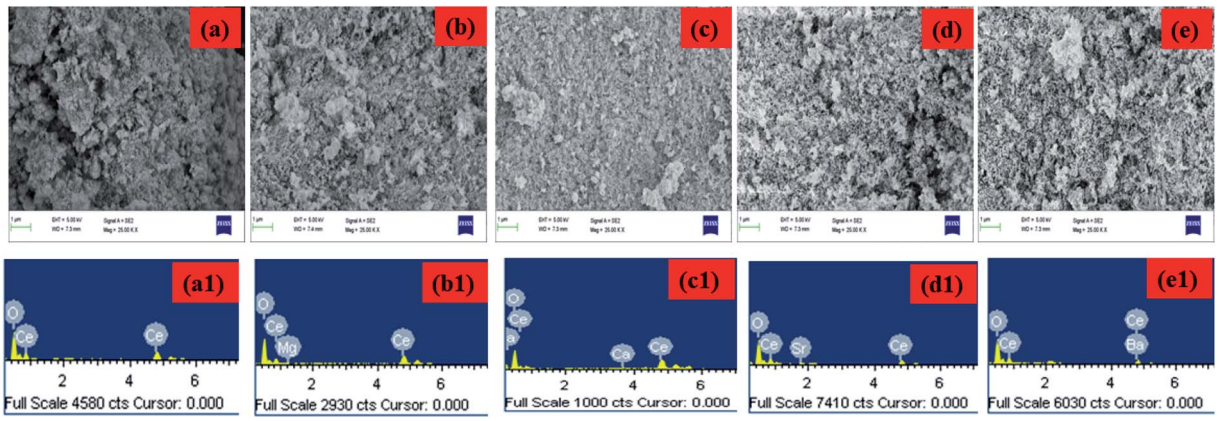

Fig. 4 (a–e) FESEM images and (a1–e1) EDX spectra of the CeO_2, MCO, CCO, SCO and BCO NMs.

the effect of the higher ionic radius of the Ba^{2+} metal ions compared to the other AMIs, namely Mg^{2+}, Ca^{2+} and Sr^{2+}.

FTIR spectroscopic studies

The FTIR spectra of the CeO_2, MCO, CCO, SCO and BCO NMs are shown in Fig. 5. The O–H peaks observed in the range of 3020–3650 cm^{-1} corresponded to the water molecules. The O–H stretching frequencies were observed at 3357, 3373, 3377, 3370 and 3375 cm^{-1} for CeO_2, MCO, CCO, SCO and BCO NMs, respectively. The asymmetric vibrations of C=O stretching were observed at wavenumbers of 1576, 1573, 1571, 1578 and 1579 cm^{-1} for the CeO_2, MCO, CCO, SCO and BCO NMs, respectively. The corresponding C–O stretching frequencies were centered at 1353, 1356, 1333, 1383 and 1369 cm^{-1} for the NMs.[29] Choudhury *et al.* reported the Ce–O–Ce stretching vibration band at 1054 cm^{-1}.[19] In the FTIR spectra, the Ce–O–Ce stretching vibrations were observed at 1058, 1057, 1058, 1058 and 1048 cm^{-1} respectively for the CeO_2, MCO, CCO, SCO and BCO NMs. In the literature, the Ce–O stretching bands have been observed in the wavenumber range between 400–1600 cm^{-1}.[30,31] In this work, the vibration frequencies of the Ce–O bands were found to be at wavenumbers (967, 946, 954 and 968 cm^{-1}), (867, 864, 878, 865 and 858 cm^{-1}), (725, 729, 740, 718 and 697 cm^{-1}) and (547, 546, 530, 548 and 545 cm^{-1}) for the CeO_2, MCO, CCO, SCO and BCO NMs, respectively.

Table 2 Elemental composition of the CeO_2, MCO, CCO, SCO and BCO NMs

	Atomic%			
Nanomaterials	Ce	O	Doping amount	Total
CeO_2	36.80	63.20	—	100%
MCO	39.90	58.54	1.56	100%
CCO	49.30	48.05	2.64	100%
SCO	26.46	72.47	1.06	100%
BCO	24.59	73.57	1.84	100%

In general, the antibacterial efficiency of NMs depends on size, surface area, polar surface and topography features. Electrostatic attraction between the positively charged NPs and negatively charged bacterial cells is also essential for the NMs to act as biocidal materials; interactions with the nanomaterial inhibits the growth of bacteria and stimulates ROS production, leading to cell death.[32–34] In particular, several studies on the photo-generation of ROS on the surfaces of metal-oxide NPs have been performed.[35,36] Light with photo-energy superior to the bandgap illuminates the NPs; the electrons (e^-) of NPs are excited through the bandgap to the conduction band, which generates holes (h^+) in the valence band.[12] The conduction band electrons and the valence band holes show high reducing and oxidizing ability. The electrons react with molecular oxygen to generate a superoxide anion ($^{\bullet}O_2^-$) *via* a reduction process. In an oxidative process, the holes can remove electrons from water

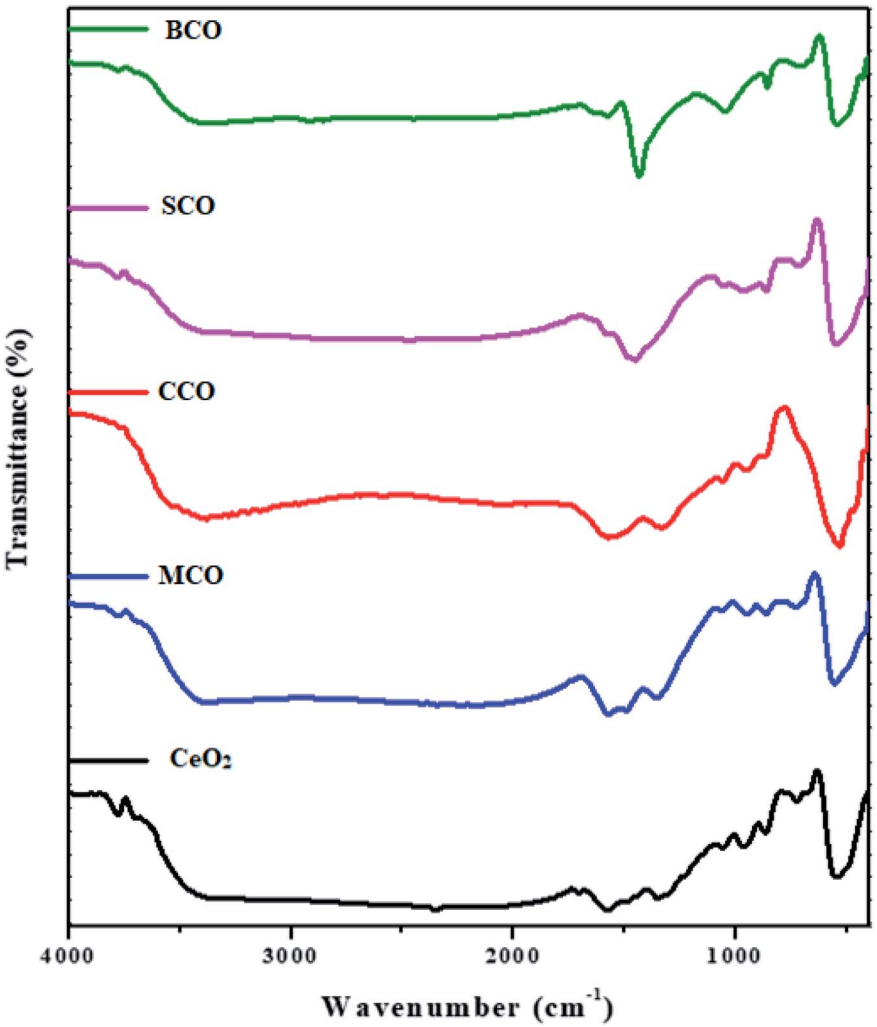

Fig. 5 Fourier transform infrared spectra of the CeO_2, MCO, CCO, SCO and BCO NMs.

molecules and hydroxyl ions to produce hydroxyl radicals ($^{\bullet}OH$).[37] As a result, singlet oxygen ($^1O_2$) is often indirectly produced from aqueous reactions. $^{\bullet}O_2^-$ and $^{\bullet}OH$ are powerful and non-selective oxidants that can affect almost all forms of organic biomolecules, including DNA, amino acids, lipids, carbohydrates, nucleic acids and proteins.[38,39] $^1O_2$ is predominantly a photocytotoxicity mediator and can irreversibly destruct treated tissues,[40] thereby causing oxidation and degradation of the bio-membrane.[41] Although $^{\bullet}O_2^-$ is not a powerful oxidant, it has important biological implications as a precursor to OH and $^1O_2$.[42] The increased ROS can be attributed to the small size of the NPs crystallites and the rise in the number of oxygen vacancies.[43]

The mechanism of ROS production in CeO_2 and BCO NMs in response to light irradiation is shown in Fig. 6. Table 3 provides information related to the feasible biocidal mechanisms of the CeO_2-based NMs against various bacterial strains. The following equations describe the formation of free radicals ($^{\bullet}OH$ and $^{\bullet}O_2^-$) in CeO_2 and the mechanism underlying the antibacterial activity of pure and BCO NMs.

$$CeO_2 + h\nu \rightarrow CeO_2(e^-) + CeO_2(h^+)$$

$$CeO_2(h^+) + H_2O \rightarrow CeO_2 + {}^{\bullet}OH^- + H^+$$

$$CeO_2(h^+) + OH^- \rightarrow CeO_2 + OH$$

$$CeO_2(e^-) + O_2 \rightarrow CeO_2 + {}^{\bullet}O_2^-$$

$$^{\bullet}O_2^- + H^+ \rightarrow HO_2{}^{\bullet}$$

$$2HO_2{}^{\bullet} \rightarrow O_2 + H_2O_2$$

UV-Visible light is used to activate the electron from the valence band to the conduction band, resulting in the generation of an electron–hole pair in both pure and BCO NMs. These holes break the H_2O molecule in the CeO_2 suspension into $^{\bullet}OH^-$ and H^+. The physisorbed oxygen molecules are converted into chemisorbed $^{\bullet}O_2^-$, which react with H^+ to produce $HO_2{}^{\bullet}$ radicals. H_2O_2 molecules are formed when HO_2 reacts with hydrogen to create hydrogen peroxide anions. The bacteria are killed by the hydrogen peroxide molecules that slowly diffuse

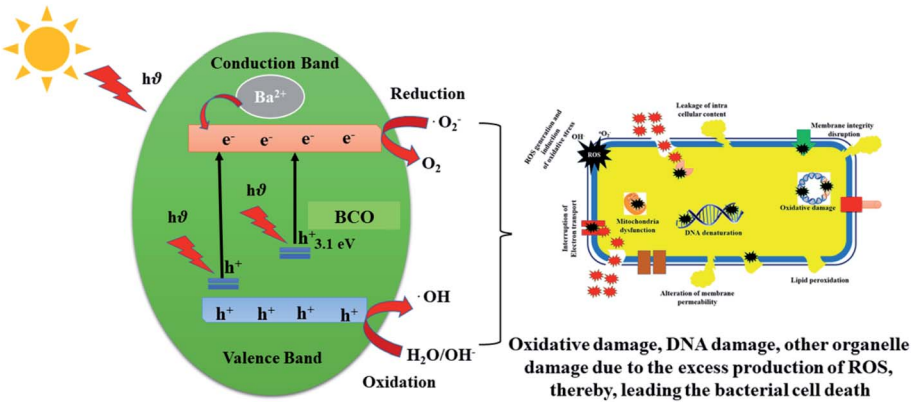

Fig. 6 The mechanism underlying ROS production in the BCO NMs in response to light irradiation.

into the cell membrane from the surface of CeO_2. However, the negatively charged hydroxyl and oxide radicals ($^{\bullet}O_2^-$) will not be transported into the cell but instead remain bound to the bacterial intracellular wall; hence these active molecules present effective bactericidal activity. The schematic representation of the interactions of pure and BCO NPs with the cell wall and DNA are shown in Fig. 7.

During the interaction of the CeO_2 NPs with bacteria, the NPs do not affect the cell structure. However, in the case of CeO_2 NPs amalgamated with Ba, after interaction with the cell wall, the additional hydroxyl radicals formed by the Ba^{2+} ions activated H_2O_2 and contributed to cell death. As Ba atom integration reduced the size of the CeO_2 NPs unlike in the CeO_2, MCO, CCO and SCO NMs, the surface area of the Ba-amalgamated CeO_2 NPs increased, making the surface more involved in light irradiation and H_2O adsorption.[13]

The disc diffusion method was employed to assay the antibacterial activities of the CeO_2, MCO, CCO, SCO and BCO NMs against *S. mutans* and *S. aureus*. A fixed concentration of 2 mg mL^{-1} was used in this study to determine the efficacy of the MCO, CCO, SCO and BCO NMs against the test species. The size of inhibition zones (mm) around the different CeO_2 NP discs is shown in Fig. 7I, and the areas of inhibition are visible in Fig. 7II. SCO and BCO NMs definitely inhibited the growth of *S. mutans* (Fig. 7II(a)) and *S. aureus* (Fig. 7II(b)). Although BCO NMs showed the highest activity of all the NMs studied, their

Table 3 The antibacterial mechanism of CeO_2 NMs with different doping materials against various bacterial strains

Nanomaterials	Bacterial name	Mechanism
Au@CeO_2	*Staphylococcus aureus*, *Escherichia coli*	The near-infrared light could significantly enhance the antibacterial activity of Au@CeO_2, and the photothermal effect did not dominate the enhancement[47]
Ce(Mn, Fe)O_2	*Staphylococcus aureus*, *Escherichia coli*	The zone of inhibition (antibacterial effect) increased with an increase in the concentration of the dopant (Mn, Fe) elements[48]
CeO_2/GO	*Escherichia coli*, *Pseudomonas aeruginosa*, *Staphylococcus aureus*, *Salmonella typhi*	CeO_2/GO showed the highest values; this confirmed that the interaction of GO and CeO_2 as a nanocomposite enhanced the antibacterial activity[49]
Sm-doped CeO_2	*Escherichia coli*, *Staphylococcus aureus*, *Bacillus cereus* and *Salmonella typhi*	The antibacterial activity revealed that the killing efficiency of Sm-CeO_2 increased with an increasing concentration of Sm^{3+}[50]
CeO_2–Al_2O_3	*Pseudomonas aeruginosa*, *Staphyloccus aureus*, *Bacillus subtilis* and *Escherichia coli*	ROS generation led to cell membrane disruption, protein denaturation, and DNA losses, hindering bacterial growth[51]
Co-doped CeO_2	*Escherichia coli*, *Staphylococcus aureus*, *Bacillus cereus* and *Salmonella typhi*	The electrostatic interactions between the positively charged nanomaterial and negatively charged bacteria aided the nanomaterial to penetrate the cell wall and cause damage[52]
CeO_2	*Escherichia coli*, *Staphylococcus aureus*, and *Pseudomonas aeruginosa*	The microorganism reduction in viable number indicates loss of inhibition ability of CeO_2 nanomaterials[53]
CeO_2/$CePO_4$	*Staphylococcus aureus*, *Bacillus cereus*, *Escherichia coli*, and *Salmonella typhimurium*	The redox switching between Ce^{3+} and Ce^{4+} in the CeO_2/$CePO_4$ nanocomposites might increase the penetrating ability of the positively charged nanocomposites through the negatively charged bacterial cell wall, causing bacterial cell damage[54]
Polyindole/Ag–CeO_2	*Staphylococcus aureus*, *Escherichia coli*	The improved antibacterial activity of the nanocomposites based on the concentration of silver ions was due to the interaction between the cell wall of the bacteria and the nanocomposites, which caused toxicity[55]
Zr-doped CeO_2	*Staphylococcus aureus*, *Escherichia coli*, *Pseudomonas aeruginosa*, *Streptococcus fecalis*, *Bacillus subtilis* and *Proteus vulgaris*	The antibacterial activity/sensitivity of the nanoparticles was associated with the different bacterial cell wall structures[56]

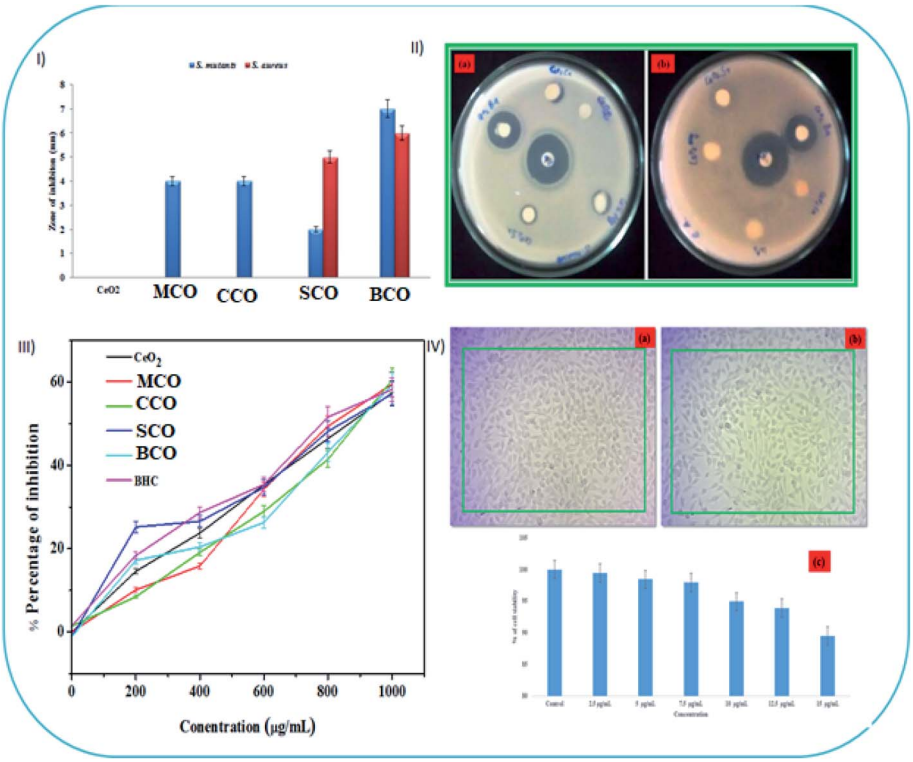

Fig. 7 (I) The antibacterial activity (zone of inhibition) of the NMs against *Streptococcus mutans* and *Staphylococcus aureus*. (II) The gradual antibacterial efficiency of the CeO_2, MCO, CCO, SCO and BCO NMs toward (a) *Streptococcus mutans* and (b) *Staphylococcus aureus*. (III) The CeO_2, MCO, CCO, SCO and BCO NMs were screened for antioxidant activity against DPPH-radical scavenging activity. (IV(a and b)) Photo images (20× magnification) reveal the topographical changes seen in the L929 fibroblast cells. (c) Toxicity tests on L929 fibroblast cells treated for 24 hours with various concentrations of BCO NMs (2.5–15 g mL^{-1}).

zones of inhibition against *S. mutans* and *S. aureus* were ~7 mm and ~6 mm, respectively. MCO and CCO NMs showed moderate activity (~4 mm) against *S. mutans* and were ineffective against *S. aureus*. It has been shown that the small crystallite size of the $BaTiO_2$ NMs induced a broad bandgap due to its redox force. Increased production of reactive oxygen species (ROS) inside the cell membranes in the presence of Ba^{2+} ions and TiO_2 NPs was observed in the case of $BaTiO_2$ NMs, resulting in improved antibacterial activity.[13] It is also worth noting that since Ba atoms can induce bacterial penetration, contact with sulphur- and phosphorus-containing compounds inside the bacterial membrane, such as deoxyribonucleic acid, causes cell death as it impedes the respiratory chain.

Often, smaller-sized NPs indeed have higher antibacterial activity than large-sized NPs. From the XRD results (Fig. 1a), the particle size of the pure and AMI-doped CeO_2 NMs, namely MCO, CCO, SCO and BCO, were found to be 5.2, 3.4 and 3.0, 3.7 and 2.3 nm, respectively. The size of BCO NMs was smaller compared with the CeO_2, MCO, CCO, SCO and BCO NMs. The small BCO NMs penetrated the microbial cell membranes due to their large interfacial area, thus displaying improved antibacterial capacity. During ROS production, the –OH group oxidizes the unsaturated fatty acids in the cell membrane, affecting the fluidity of the cell membrane. The bandgap energies of the CeO_2, MCO, CCO, SCO and BCO NMs were observed to be 2.85, 2.9, 2.95, 3.0 and 3.1 eV, respectively. In comparison with the CeO_2, MCO, CCO and SCO NMs, the band difference of the BCO NMs was the largest, which was a significant factor in its ROS-mediated toxicity. The presence of barium in the CeO_2 matrix led to a substantial decrease in the number of viable bacteria.

Since Ba ions interact with protein thiol groups, respiratory enzymes are inactivated, resulting in the formation of more ROS. The bandgap behavior of CeO_2 NPs plays a crucial role in the toxicity caused by ROS. Ba causes many oxygen atoms to be adsorbed on the surface of CeO_2, releasing more ROS in the suspension and putting the bacteria under intense oxidative stress, thus raising the antibacterial action of the BCO NMs. The PL spectra showed that the green emission wavelengths of BCO NMs were ~513 nm and ~542 nm, while the observed green emission wavelengths for CeO_2 NMs were ~509 nm and ~539 nm. This demonstrates that the BCO NMs had more oxygen vacancies than CeO_2 NPs, resulting in more ROS. Other potential mechanisms may include the interaction of the NMs with biological macromolecules, such as carbohydrates, lipids, proteins and nucleic acid. It is known that the bacterial cells carry a negative charge, while the metal oxides are positively charged.[44] This results in an electromagnetic attraction between the microbes and the treated surface. When contact is made, the microbe immediately becomes oxidized and dies. The oxidative stress caused by ROS generation would establish the needed intracellular functional modifications, leading to cell

death. The NPs are thought to release metal ions that interact with the –SH groups of the proteins protruding through the microbial cell membranes,[45] allowing nutrients to pass through the cell wall. The NM inactivates these proteins, thereby reducing membrane permeability and ultimately leading to cell death.[9]

In the clinical field, bactericidal agents are highly favored because they result in a higher recovery rate from microbial infections.[46] The MIC and MBC results of SCO and BCO NMs against *S. mutans* and *S. aureus* are given in Table 4. Fig. SI1 and SI2† show that 100% cell growth was present in the control bacterial culture. The percentage of bacterial cell growth decreased on increasing the concentrations (200, 400, 600, 800, 1000, 1500 and 2000 μg mL^{-1}) of the SCO and BCO NMs. The MBC values of the SCO and BCO NMs against *S. mutans* were 1500 and 1000 μg mL^{-1}, respectively, while the MBC values of the SCO and BCO NMs treated with *S. aureus* were 2000 and 1500 μg mL^{-1}, respectively, as seen in Table 4. The minimum amount of BCO required to inhibit bacterial growth was observed as 600 and 800 μg mL^{-1} for *S. mutans* and *S. aureus*, respectively.

The bandgap activity of CeO_2, MCO, CCO, SCO and BCO NMs was a significant factor in ROS-mediated toxicity. The UV-vis tests revealed that the bandgap of CeO_2, MCO, CCO, SCO and BCO NMs was 2.85, 2.9, 2.95, 3.0, and 3.1 eV, respectively. When compared with CeO_2, MCO, CCO and SCO NMs, the bandgap of BCO NMs increased. It was discovered that Ba caused a higher amount of oxygen atoms to be adsorbed on the surface of CeO_2, resulting in more ROS in the suspension and hence the density of oxidative stress on the bacteria; hence, CeO_2 NPs doped with Ba enhanced the antibacterial response. Antioxidants or free-radical scavengers are substances that can effectively scavenge or slow down the cell damage caused by free radicals.[36] The DPPH assay of CeO_2, MCO, CCO, SCO, BCO, and butylated hydroxytoluene is shown in Fig. 4III, and they all showed free-radical-scavenging ability. An increase in the concentrations of CeO_2, MCO, CCO, SCO and BCO NMs increased the inhibition percentage. CeO_2, MCO, CCO, SCO and BCO, as well as butylated hydroxytoluene, displayed radical-scavenging activities at concentrations 200 to 1000 g mL^{-1}, with activity percentages of 57.4%, 55.9%, 51.68%, 65.51%, 67.96% and 49.68%, respectively. BCO NMs showed better scavenging characteristics than the other CeO_2 NMs. Smaller sized NMs exhibit potential against tested bacteria due to the larger surface area and higher antioxidant activity than bigger sized NMs. The particle sizes of CeO_2, MCO, CCO, SCO and BCO NMs were found to be 5.2, 3.4, 3.0, 3.7, and 2.3 nm, respectively, based on XRD results. The BCO NM size was reduced compared to CeO_2, MCO, CCO and SCO NMs. Conversely, it was determined from the analysis that BCO NM exhibited improved biocompatibility, scavenging activity, and biocidal properties, and it can surely be used in the healthcare industry, especially in the biomedical field. The *in vitro* cytotoxicity assay of BCO on L929 cells showed some surface morphological changes under a light microscope, as shown in Fig. 7IV(a and b). The untreated control cells revealed a uniform fusiform structure (cell viability of 100%) and did not exhibit injury to the cell membrane (Fig. 7IV(a)). On the surface of the fibroblasts, there is the formation of a uniform fusiform BCO NM structure (Fig. 7IV(b)) (cell viability of 89.45%) (Fig. 7IV(c)). This result showed that the BCO NM exhibited a minimum toxicity percentage in comparison with the control group. However, BCO is a potential and important NM as a non-toxic additive suitable for advanced cosmetic skin-care products and clinical applications in the medical field.[36]

Table 4 The MIC and MBC values of SCO and BCO against *S. mutans* and *S. aureus*

	S. mutans		*S. aureus*	
Compound	MIC (mg mL^{-1})	MBC (mg mL^{-1})	MIC (mg mL^{-1})	MBC (mg mL^{-1})
SCO	1	1.5	1	2
BCO	0.6	1	0.8	1.5

Conclusions

In this investigation, CeO_2, MCO, CCO, SCO and BCO NMs were successfully prepared *via* the precipitation method. The XRD analysis revealed that CeO_2, MCO, CCO, SCO and BCO NMs exemplified the cubic fluorite crystal structure of CeO_2 with the mean crystallite sizes of 5.2, 3.4 3.0, 3.7 and 2.3 nm, respectively. The FESEM images exhibited that the morphology of CeO_2 NMs was spherical, whereas the MCO, CCO, SCO and BCO NMs exhibited needle-like structures. The elemental compositions of the CeO_2, MCO, CCO, SCO and BCO NMs were estimated through EDAX. In the FTIR spectra, the Ce–O stretching bands appeared at wavenumbers 547, 546, 530, 548 and 545 cm^{-1} for CeO_2, MCO, CCO, SCO and BCO NMs, respectively. The absorption edge peaks of the CeO_2, MCO, CCO, SCO and BCO NMs were observed in the UV-vis spectra at ~435, ~427, ~420, ~413, and ~399 nm, respectively. Because of the photo-excitation of an electron from the valence band to the conduction band, the PL results revealed that the emission peaks of the MCO, CCO, SCO and BCO NMs had moved compared with that of CeO_2 NPs. Further, the antibacterial activity of BCO NMs was found to be higher those that of the CeO_2, MCO, CCO, and SCO NMs. The antibacterial effect was mainly due to the ROS of the CeO_2 NPs, and hence, the BCO NM exhibited less toxicity toward healthy fibroblast cells (L929). These NMs will be useful in biomedical applications, including the treatment of dental caries, infective endocarditis, and bloodstream infections that can infect almost any site in the human body and bones.

Conflicts of interest

The authors reported no declarations of interest.

Acknowledgements

The authors (CK and KVP) received support from the Fondecyt Postdoctoral Project 3190029, Centro de Investigación de

Polímeros Avanzados (CIPA), ANID/CONICYT Regional and GORE BIO-BIO R17A10003, Chile. The author (SN) received funding support from Bishop Heber College management (BHC: F.NO:MRP/1002/2020), Trichy, Tamil Nadu, India.

References

1 V. Kanikireddy, K. Varaprasad, T. Jayaramudu, C. Karthikeyan and R. Sadiku, *Int. J. Biol. Macromol.*, 2020, **164**, 963–975.
2 K. Varaprasad, C. Karthikeyan, V. KanikiReddy, D. Núñez, E. R. Sadiku and R. Briones, *Antibiotic Nanomaterials*, Elsevier Inc., 2020.
3 G. Franci, A. Falanga, S. Galdiero, L. Palomba, M. Rai, G. Morelli and M. Galdiero, *Molecules*, 2015, **20**, 8856–8874.
4 M. Feng, Y. Fang, C. Ma, X. Duan, Y. Zhang, B. Han, H. Hu, L. Meng, F. Wang and J. Li, *Biomolecules*, 2021, **11**, 1–17.
5 R. Wise, M. Blaser, O. Carrs, G. Cassell, N. Fishman, R. Guidos, S. Levy, J. Powers, R. Norrby, G. Tillotson, R. Davies, S. Projan, M. Dawson, D. Monnet, M. Keogh-Brown, K. Hand, S. Garner, D. Findlay, C. Morel, R. Wise, R. Bax, F. Burke, I. Chopra, L. Czaplewski, R. Finch, D. Livermore, L. J. V. Piddock and T. White, *J. Antimicrob. Chemother.*, 2011, **66**, 1939–1940.
6 L. M. Estes, P. Singha, S. Singh, T. S. Sakthivel, M. Garren, R. Devine, E. J. Brisbois, S. Seal and H. Handa, *J. Colloid Interface Sci.*, 2021, **586**, 163–177.
7 Y. H. Lin, L. J. Shen, T. H. Chou and Y. hsin Shih, *J. Cluster Sci.*, 2021, **32**, 405–413.
8 V. Baldim, F. Bedioui, N. Mignet, I. Margaill and J. F. Berret, *Nanoscale*, 2018, **10**, 6971–6980.
9 A. Arumugam, C. Karthikeyan, A. S. Haja Hameed, K. Gopinath, S. Gowri and V. Karthika, *Mater. Sci. Eng., C*, 2015, **49**, 408–415.
10 P. Tamizhdurai, S. Sakthinathan, S. M. Chen, K. Shanthi, S. Sivasanker and P. Sangeetha, *Sci. Rep.*, 2017, **7**, 1–13.
11 A. F. Halbus, T. S. Horozov and V. N. Paunov, *Adv. Colloid Interface Sci.*, 2017, **249**, 134–148.
12 L. Brunet, D. Y. Lyon, E. M. Hotze, P. J. J. Alvarez and M. R. Wiesner, *Environ. Sci. Technol.*, 2009, **43**, 4355–4360.
13 K. Vijayalakshmi and D. Sivaraj, *RSC Adv.*, 2016, **6**, 9663–9671.
14 L. Li, H. K. Yang, B. K. Moon, Z. Fu, C. Guo, J. H. Jeong, S. S. Yi, K. Jang and H. S. Lee, *J. Phys. Chem. C*, 2009, **113**, 610–617.
15 S. Deshpande, S. Patil, S. V. Kuchibhatla and S. Seal, *Appl. Phys. Lett.*, 2005, **87**, 1–3.
16 W. Lee, S.-Y. Chen, E. Tseng, A. Gloter and C.-L. Chen, *J. Phys. Chem. C*, 2016, **120**, 14874–14882.
17 H. Pan, Y. Zhu, H. Sun, Y. Feng, C. H. Sow and J. Lin, *Nanotechnology*, 2006, **17**, 5096–5100.
18 T. Masui, K. Fujiwara, K. I. Machida, G. Y. Adachi, T. Sakata and H. Mori, *Chem. Mater.*, 1997, **9**, 2197–2204.
19 B. Choudhury and A. Choudhury, *Mater. Chem. Phys.*, 2012, **131**, 666–671.
20 E. Shoko, M. F. Smith and R. H. McKenzie, *J. Phys.: Condens. Matter*, 2010, **22**, 223201.
21 A. H. Morshed, M. E. Moussa, S. M. Bedair, R. Leonard, S. X. Liu and N. El-Masry, *Appl. Phys. Lett.*, 1997, **70**, 1647–1649.
22 N. Serpone, *J. Phys. Chem. B*, 2006, **110**, 24287–24293.
23 D. D. Koelling, A. M. Boring and J. H. Wood, *Solid State Commun.*, 1983, **47**, 227–232.
24 C. A. Hogarth and Z. T. Al-Dhhan, *Phys. Status Solidi*, 1986, **137**, K157–K160.
25 L. Wang, J. Ren, X. Liu, G. Lu and Y. Wang, *Mater. Chem. Phys.*, 2011, **127**, 114–119.
26 X. H. Lu, X. Huang, S. L. Xie, D. Z. Zheng, Z. Q. Liu, C. L. Liang and Y. X. Tong, *Langmuir*, 2010, **26**, 7569–7573.
27 C. G. Kim, *Appl. Phys. Lett.*, 2001, **79**, 3047–3049.
28 Y. Huang, Y. Cai, D. Qiao and H. Liu, *Particuology*, 2011, **9**, 170–173.
29 L. S. Reddy Yadav, K. Manjunath, B. Archana, C. Madhu, H. Raja Naika, H. Nagabhushana, C. Kavitha and G. Nagaraju, *Eur. Phys. J. Plus*, 2016, **131**, 154.
30 G. Wang, Q. Mu, T. Chen and Y. Wang, *J. Alloys Compd.*, 2010, **493**, 202–207.
31 S. Phoka, P. Laokul, E. Swatsitang, V. Promarak, S. Seraphin and S. Maensiri, *Mater. Chem. Phys.*, 2009, **115**, 423–428.
32 T. Xia, M. Kovochich, J. Brant, M. Hotze, J. Sempf, T. Oberley, C. Sioutas, J. I. Yeh, M. R. Wiesner and A. E. Nel, *Nano Lett.*, 2006, **6**, 1794–1807.
33 E. Burello and A. P. Worth, *Nanotoxicology*, 2011, **5**, 228–235.
34 T. Xia, M. Kovochich, M. Liong, L. Mädler, B. Gilbert, H. Shi, J. I. Yeh, J. I. Zink and A. E. Nel, *ACS Nano*, 2008, **2**, 2121–2134.
35 N. Sisubalan, V. S. Ramkumar, A. Pugazhendhi, C. Karthikeyan, K. Indira, K. Gopinath, A. S. H. Hameed and M. H. G. Basha, *Environ. Sci. Pollut. Res.*, 2018, **25**, 10482–10492.
36 C. Karthikeyan, S. Natarajan, S. Mani, K. Varaprasad, G. B. M. Hussain, S. Wang and R. Sadiku, *J. Hazard. Mater.*, 2021, 124884.
37 H. F. Lin, S. C. Liao and S. W. Hung, *J. Photochem. Photobiol., A*, 2005, **174**, 82–87.
38 S. Tsunekawa, J. T. Wang, Y. Kawazoe and A. Kasuya, *J. Appl. Phys.*, 2003, **94**, 3654–3656.
39 J. Du and J. M. Gebicki, *Int. J. Biochem. Cell Biol.*, 2004, **36**, 2334–2343.
40 S. Wang, R. Gao, F. Zhou and M. Selke, *J. Mater. Chem.*, 2004, 487–493.
41 R. Bakalova, H. Ohba, Z. Zhelev, M. Ishikawa and Y. Baba, *Nat. Biotechnol.*, 2004, **22**, 1360–1361.
42 I. Fridovich, *Sci. Am.*, 1986, **247**, 1–11.
43 J. Becker, K. R. Raghupathi, J. St. Pierre, D. Zhao and R. T. Koodali, *J. Phys. Chem. C*, 2011, **115**, 13844–13850.
44 P. Hosseinkhani, A. M. Zand, S. M. ImaniRezyi and S. Rezaei Zarchim, *Int. J. Nano Dimens.*, 2011, **1**, 279–285.
45 G. X. Tong, F. F. Du, Y. Liang, Q. Hu, R. N. Wu, J. G. Guan and X. Hu, *J. Mater. Chem. B*, 2013, **1**, 454–463.
46 G. L. French, *J. Antimicrob. Chemother.*, 2006, **58**, 1107–1117.
47 C. Liu, M. Zhang, H. Geng, P. Zhang, Z. Zheng, Y. Zhou and W. He, *Appl. Catal., B*, 2021, **295**, 120317.

48 M. Moazzam, A. Haq, F. Amin, M. Ajaz-un-nabi, I. Khan and N. Sabir, *Phys. B*, 2021, **600**, 412562.
49 G. Sharma, D. Prema, K. S. Venkataprasanna, J. Prakash, S. Sahabuddin and G. Devanand Venkatasubbu, *Arabian J. Chem.*, 2020, **13**, 7680–7694.
50 A. Balamurugan, Y. S. K. M Sudha, S. Surendhiran, R. Anandarasu and S. Ravikumar, *Mater. Today: Proc.*, 2020, 3588–3594.
51 D. A. Al Farraj, A. M. Al-Mohaimeed, R. M. Alkufeidy and N. A. Alkubaisi, *Colloid Interface Sci. Commun.*, 2021, **41**, 100375.
52 K. Hamidian, A. Najafidoust, A. Miri and M. Sarani, *Mater. Res. Bull.*, 2021, **138**, 111206.
53 S. A. Abid, A. A. Taha, R. A. Ismail and M. H. Mohsin, *Environ. Sci. Pollut. Res.*, 2020, **27**, 30479–30489.
54 M. Noor, M. A. Al Mamun, A. K. M. Atique Ullah, A. Matsuda, G. Kawamura, M. A. Hakim, M. F. Islam and M. A. Matin, *J. Phys. Chem. Solids*, 2021, **148**, 109751.
55 M. Elango, M. Deepa, R. Subramanian and G. Saraswathy, *Mater. Today: Proc.*, 2020, **26**, 3544–3551.
56 R. Bakkiyaraj, M. Balakrishnan, G. Bharath and N. Ponpandian, *J. Alloys Compd.*, 2017, **724**, 555–564.